Available online at www.sciencedirect.com

ScienceDirect

journal homepage: www.elsevier.com/locate/he

Production of CO-rich hydrogen from methane dry reforming over lanthania-supported cobalt catalyst: Kinetic and mechanistic studies

Bamidele V. Ayodele [a], *Maksudur R. Khan* [a], *Su Shiung Lam* [c], *Chin Kui Cheng* [a,b,*]

[a] *Faculty of Chemical & Natural Resources Engineering, Universiti Malaysia Pahang, Lebuhraya Tun Razak, 26300 Gambang Kuantan, Pahang, Malaysia*

[b] *Rare Earth Research Centre, Universiti Malaysia Pahang, Lebuhraya Tun Razak, 26300 Gambang Kuantan, Pahang, Malaysia*

[c] *Eastern Corridor Renewable Energy Group (ECRE), School of Ocean Engineering, Universiti Malaysia Terengganu, 21030 Kuala Terengganu, Terengganu, Malaysia*

ARTICLE INFO

Article history:
Received 4 December 2015
Received in revised form
17 January 2016
Accepted 18 January 2016
Available online 10 February 2016

Keywords:
Cobalt
Dry reforming
Methane
Lanthanum
Langmuir–Hinshelwood
Syngas

ABSTRACT

In this study, the production of CO-rich hydrogen from methane dry reforming over lanthania-supported Co catalyst was investigated. The Co/La_2O_3 catalyst was synthesized via wet-impregnation method and characterized using instrument techniques such as TGA, FTIR, XRD, FESEM-EDX and N_2 adsorption-desorption analysis. The catalytic activity of the Co/La_2O_3 catalyst tested in a fixed bed stainless steel reactor yielded highest CH_4 and CO_2 conversion of 50% and 60% respectively at 1023 K and feed ratio of 1.0. The methane dry reforming reaction gave highest H_2 and CO yield of 45% and 58% respectively. Furthermore, kinetics and mechanistic behavior of the La_2O_3 supported Co catalyst in methane dry reforming reaction was investigated as a function of temperature and partial pressure of reactants (CH_4 and CO_2). The experimental data obtained from the kinetics measurements were fitted using the empirical power-law rate expression, as well as six different Langmuir–Hinshelwood kinetics models. The six models were then statistically and thermodynamically discriminated. Consequently, the Langmuir–Hinshelwood kinetics model (dual-site associative adsorption of both CH_4 and CO_2 with bimolecular surface reaction) was adjudged the best representative model. Activation energy values of 96.44 and 98.11 kJ mol^{-1} were obtained for the CH_4 consumptions from the power-law and Langmuir–Hinshelwood models, respectively. A lower activation energy of *circa* 72 kJ mol^{-1} obtained for CO_2 consumption showed that the rate of consumption of CO_2 consumption was speedier than CH_4.

* *Corresponding author*. Faculty of Chemical & Natural Resources Engineering, Universiti Malaysia Pahang, Lebuhraya Tun Razak, 26300 Gambang Kuantan, Pahang, Malaysia. Tel.: +60 9 5492896; fax: +60 9 5492889.
E-mail address: chinkui@ump.edu.my (C.K. Cheng).

http://dx.doi.org/10.1016/j.ijhydene.2016.01.091

Introduction

Increasing environmental awareness in the last four decades has attracted a lot of attentions on dry reforming of methane [1]. Dry reforming of methane which involves the catalytic reaction of CO_2 and CH_4 has been reported as a good alternative for the production of synthesis gas (syngas), a mixture of hydrogen (H_2) and carbon monoxide (CO) [2,3]. Thus far, commercial production of syngas has been mainly by methane steam reforming over Ni or Fe supported catalyst [4]. However, this process is a major contributor to the emission of CO_2 via water gas shift reaction [5]. The CO_2 released during this process is a key component of greenhouse gases which are responsible for global warming via "greenhouse effect" [2]. Besides that, high syngas ratio from the process is not suitable for use as chemical intermediate for Fischer-Tropsch synthesis (FTS) [6]. On the contrary, methane dry reforming has both environmental and energy benefits. Methane and CO_2, which are two major contributors to greenhouse gases, are utilized during the reforming reaction producing low syngas ratio (<2) [7,8]. The syngas produced is the main chemical building block for production of valuable oxygenated fuels via FTS [9,10].

In spite of the environmental and energy advantages of methane dry reforming process, catalyst deactivation from sintering and coking have been the major challenges hindering the full development of the process [11,12]. As a result of these constraints, methane dry reforming has been investigated over several supported metal catalysts such as Pt, Pd, Ru, Rh, Ir, Co and Ni [13]. An extensive review on methane dry reforming over noble metal catalysts by Pakhare and Spivey [13] concludes that noble metals such as Pt, Ru and Rh are more resistant to carbon deposition compared to other metals but expensive. Although, Ni and Co catalysts are less resistant to carbon depositions compared to the noble metals, they are inexpensive [7]. The resistivity of these metals to carbon deposition can be improved on by an addition of small amount of noble metals and basic oxides as promoters, as well as using rare earth metal oxides such as, CeO_2, and La_2O_3 as supports [14–16]. According to report by Sato et al. [17], rare earth metal oxides possess basic surface characteristic which makes them efficient for CO_2 activation. Moreover, the high oxygen storage capacity exhibited by rare earth metal oxides enhanced catalyst stability through the oxidation of the carbon formed from the methane dry reforming [18].

Kinetics and mechanistic studies of methane dry reforming to syngas has been investigated over rare earth supported noble metals and Ni catalysts in order to mitigate carbon formation and other mechanisms of deactivation [19,20]. Munera et al. [20] reported that both CH_4 and CO_2 were adsorbed on Rh/La_2O_3 catalyst. The authors proposed the dissociation of the adsorbed CH_4 as the rate determining step producing C and H_2. Furthermore, CO_2 was observed to adsorb on the La_2O_3 basic site providing surface oxygen for the gasification of deposited carbon. Recently, Pakhare et al. [21] investigated the kinetics and mechanistic study of methane dry reforming over Rh-substituted $La_2Zr_2O_7$ pyrochlores catalyst. The authors proposed reaction mechanism that was in accordance with that of Munera et al. [20]. However, reverse water gas shift reactions as well as activation of the adsorbed CH_4 were proposed as the rate determining step.

Kinetics and mechanistic study of methane dry reforming over La_2O_3 supported Ni catalysts have been widely reported in literature [22,23]. The proposed mechanisms for the methane dry reforming by these authors was either single site or dual site rate determining steps with activation of CH_4 by the metal Ni and C gasification by adsorbed CO_2 on the support site as the rate determining steps. Langmuir–Hinshelwood kinetics model was developed based on these mechanisms and the experimental data were fitted into the kinetics model. The findings reported by these authors showed that the predicted rates of CH_4 consumption obtained from the kinetics model were in good agreement with the experimental data which makes the proposed mechanisms plausible. Significantly, to the best of our knowledge, kinetics and mechanistic studies of methane dry reforming to syngas over La_2O_3-supported Co catalyst have not been reported.

Therefore, the present study focuses on the production of CO-rich hydrogen from methane dry reforming over lanthania (La_2O_3) supported cobalt catalyst. Furthermore, the kinetics and mechanistic studies of the methane dry reforming over the La_2O_3-supported Co catalyst was also reported. The 20wt%Co/80wt%La_2O_3 catalyst was synthesized by wet impregnation and characterized using various instrumental techniques. The kinetics measurement of the methane dry reforming over the as-synthesized catalyst was done under atmospheric conditions in the temperatures that ranged 923–1023 K. Langmuir–Hinshelwood kinetics model was developed considering both single- and dual-site adsorption of CH_4 and CO_2.

Experimental

Preparation of catalyst

Prior to the preparation of the 20wt%Co/80wt%La_2O_3 catalyst, the La_2O_3 support was synthesized by thermal decomposition of $La(NO_3)_3{\cdot}6H_2O$ (99.99% purity, Sigma–Aldrich) at 873 K for 2 h [24]. The as-prepared La_2O_3 support was impregnated with aqueous solution of $Co(NO_3)_2{\cdot}6H_2O$ (99.99% purity, Sigma–Aldrich) equivalent to 20wt% Co loading. The choice of 20% Co loading was based on the findings by Jacobs et al. [25] and Ma et al. [26] who investigated the effect of Co-metal loading (7.5%–20% Co) on catalytic performance of supported Co-catalysts and concluded that the catalyst with 20% Co loading showed the best performance. The slurry from the mixture of the La_2O_3 powder and the aqueous solution of $Co(NO_3)_2{\cdot}6H_2O$ (20% Co loading) was continuously stirred for 3 h to allow for aging of the Co precursor. This was followed by drying the slurry at 393 K for 24 h and calcination at 873 K for 6 h to give an unreduced 20wt%Co/80wt%La_2O_3 catalyst. The gaseous species used in this study were CH_4 (99.99% purity), CO_2 (99.99% purity), H_2 (99.99% purity) and N_2 (99.99% purity).

Catalyst characterization

The thermal calcination profiles of the uncalcined (dried only) 20wt%Co/80wt%La_2O_3 catalyst as a function of temperature at constant heating rates (10, 15 and 20 K/min) were obtained

using thermogravimetric analyzer (TGA), TA instrument Q500. The $La(NO_3)_3{\cdot}6H_2O$ and the synthesized Co/La_2O_3 catalyst were analyzed using Thermo Scientific FTIR spectrometer (Nicolet iS 50). Both samples were analyzed using attenuated total reflectance (ATR) method over wave number ranged 4000–400 cm^{-1} at scanning rate of 0.02 cm^{-1}. The spectra were collected, processed and analyzed using Omnic series spectra analysis software.

The crystalline structure of the calcined, as well as the reduced fresh 20wt%Co/80wt%La_2O_3 catalyst were measured by X-ray powder diffraction spectroscopy. The XRD analysis was performed using Rigaku Miniflex II diffractometer (CuKα radiation with $\lambda = 0.154$ nm). The XRD pattern of the catalysts was collected within 2θ range of 10°–80° at a scanning step of 0.02°. The textural properties of the fresh catalyst were measured by N_2 adsorption-desorption isotherm at 77 K using Thermo Scientific Surfer Analyzer in line with the standard BET procedure [27]. The sample was degassed at 523 K for 3 h prior to the analysis. The pore size distribution of the catalyst was estimated from the N_2 desorption data using Barret-Joyner-Halenda (BJH) analysis [28]. The morphology and elemental composition of the unreduced fresh catalyst was performed using JEOL field emission scanning electron microscopy (FESEM) (JSM-7800F) equipped with energy dispersive X-ray spectroscopy (EDX).

Catalytic tests

The catalytic test was performed in a stainless steel fixed bed reactor (ID: 10 mm and length: 35 cm). The reactor loaded with 200 mg of 20wt%Co/80wt%La_2O_3 catalyst supported on quartz wool, was placed in a tube-furnace equipped with four heating zones. The temperature of the catalytic bed was monitored using a Type-K thermocouple. The catalyst was reduced *in situ* under a flow of 60 ml/min H_2/N_2 (1:5) for 1 h at 973 K. Subsequently, the reduced catalyst was purged in a flow of 50 ml/min N_2 for 20 min. The outlet gas composition consisting of the products (H_2 and CO) and the reactants (CO_2 and CH_4) were analyzed using gas chromatography (GC) instrument (Agilent GC system 6890 N Series) equipped with thermal conductivity detector (TCD). The GC system consists of two packed columns, namely Supelco Molecular Sieve 13 × (10 ft × 1/8 in OD × 2 mm ID, 60/80 mesh, Stainless Steel) and Agilent Hayesep DB (30 ft × 1/8 in OD × 2 mm ID, 100/120 mesh, Stainless Steel). Helium gas with a flowrate of 20 ml min^{-1} was used as the carrier gas at the operating column temperature of 393 K. The conversions of the CH_4 and CO_2 as well as the yields of H_2 and CO are calculated based on the expressions in Eqs. (1)–(4) respectively.

$$CH_4 \text{ conversion } (\%) = \frac{F_{CH_{4in}} - F_{CH_{4out}}}{F_{CH_{4in}}} \times 100 \quad (1)$$

$$CO_2 \text{ conversion } (\%) = \frac{F_{CO_{2in}} - F_{CO_{2out}}}{F_{CO_{2in}}} \times 100 \quad (2)$$

$$H_2 \text{ yield} = \frac{F_{H_{2out}}}{2F_{CH_{4in}}} \times 100 \quad (3)$$

$$CO \text{ yield} = \frac{F_{CO_{out}}}{F_{CH_{4in}} + F_{CO_{2in}}} \times 100 \quad (4)$$

Kinetics measurements

The kinetics experiment was performed by varying the partial pressure of CH_4 from 5 to 50 kPa at a fixed CO_2 partial pressure (50 kPa) and vice versa. The partial pressure of the inert gas (N_2) was kept constant in both cases. The reaction rate was estimated from Eqs. (5) and (6) using the reaction data that were collected from temperatures that ranged 923–1023 K in a constant gas hourly space velocity (GHSV) of 30,000 h^{-1} under controlled atmospheric condition

$$r_i = \frac{y_{io}\dot{n}_{io} - y_i\dot{n}_i}{W_{cat}} \quad \text{for } i = CH_4 \text{ and } CO_2 \quad (5)$$

$$r_i = \frac{y_i\dot{n}_i}{W_{cat}} \quad \text{for } i = H_2 \text{ and CO} \quad (6)$$

where r_i is the rate of consumption of the reactants or rate of formation of the products; y_{io} and y_i are the mole fraction of species in the inlet and outlet streams, respectively; $\dot{n}_{io}$ is the molar flowrate of the total moles of gases in the inlet stream and $\dot{n}_i$ is the molar flowrate of the total moles of gases in the outlet stream; W_{cat} is the weight of catalyst.

Results and discussion

Fresh catalyst characterization

The FTIR spectra of the $La(NO_3)_3{\cdot}6H_2O$ in comparison with the synthesized Co/La_2O_3 catalyst is depicted in Fig. 1. Significantly, four types of bonds namely O–H, N–O, C–O and M–O can be identified from the FTIR spectra of the La-precursor. The O–H stretching bond within wavenumber ranged 3386–3526 cm^{-1} can be attributed to the presence of physical and hydrated water. The NO bond at wavenumber ranged 3185–3238 cm^{-1} corresponds to the presence of nitrate

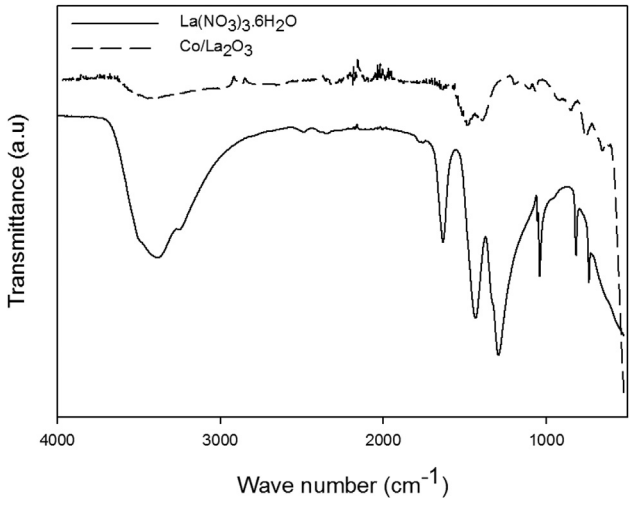

Fig. 1 – FTIR analysis of the 20wt%Co/80wt%La_2O_3 catalyst and La-precursor.

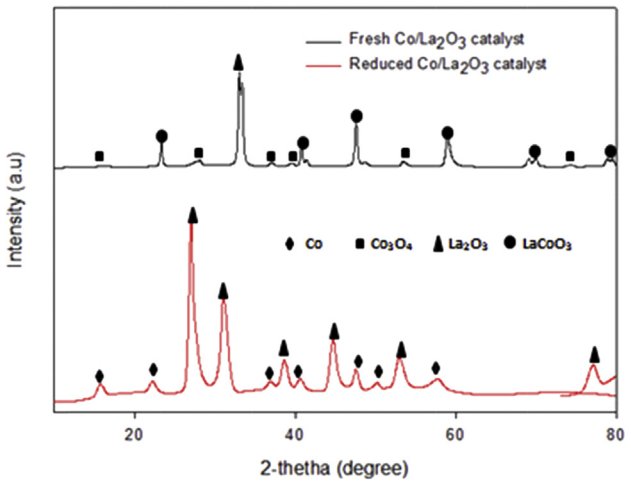

Fig. 2 – XRD powder diffraction pattern of the freshly-calcined and -reduced 20wt%Co/80wt%La_2O_3 catalyst.

species in the precursor. The CO and MO bond at wavenumber ranged 1288–1644 cm^{-1} and 629–652 cm^{-1} respectively can be attributed to dissolve atmospheric CO_2 and the La-metal-O stretching vibration. The spectra of the Co/La_2O_3 catalyst obtained show the disappearance of NO and OH bond signifying the removal of the physical and hydrated water, as well as the decomposition of the nitrate species. The presence of the peaks at wavenumber 629–652 cm^{-1} corresponds to the formation of the respective La_2O_3 which is corroborated by the XRD pattern of the calcined 20wt%Co/80wt%La_2O_3 catalyst depicted in Fig. 2. Overall, the XRD pattern of the unreduced calcined catalyst reveals the formation of Co_3O_4, La_2O_3 and Perovskite $LaCoO_3$ species. The formation of $LaCoO_3$ can be attributed to the strong interaction between Co and La_2O_3 support. The diffraction peaks at $2\theta = 16.10°$, 28.10°, 37.07°, 39.63°, 48.73° and 74.48° can be assigned to the spinel phase of Co_3O_4 while the body center cubic phase of $LaCoO_3$ crystalline phase can be identified at $2\theta = 23.30°$,41.46°, 47.58°, 58.97°, 69.11°, 70.01° and 79.52°, respectively. The peak identified at $2\theta = 33.42°$ can be attributed to hexagonal structure of La_2O_3 species. The reduction of the catalysts resulted in the formation of face cubic and hexagonal structure of the pure Co° metal and La_2O_3 species, respectively. This observation is consistent with the findings of Pereñiguez et al. [29] who identified NiO and $LaNiO_3$ species in the XRD pattern of Ni/La_2O_3 catalyst before reduction as well as Ni° and La_2O_3 species after reduction. The estimation of the crystallite size of the Co° species from Scherer's equation using full-width-half-maximum (FWHM) of the respective XRD peak (1 1 1) gives 6.99 nm.

The FESEM micrograph and EDX analysis showing the morphology and the elemental compositions of the 20wt%Co/80wt%La_2O_3 catalyst is depicted in Figs. 3 and 4, respectively. The FESEM images show irregular-shaped nano-rods

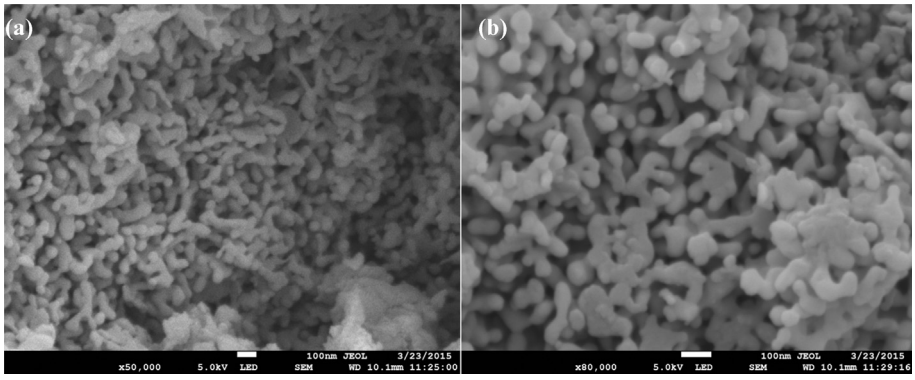

Fig. 3 – FESEM micrograph of the fresh 20wt%Co/80wt%La_2O_3 catalyst at (a) × 50,000 magnification, and (b) × 80,000 magnification.

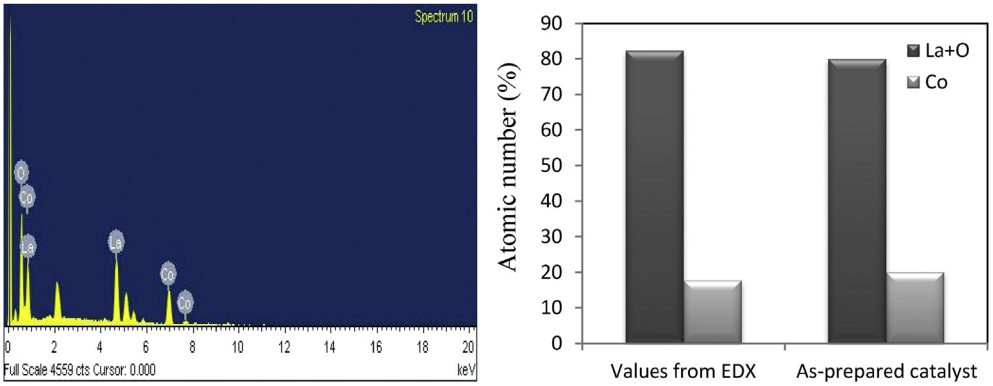

Fig. 4 – Elemental composition of the as-prepared fresh 20wt%Co/80wt%La_2O_3 catalyst from EDX dot mapping.

Table 1 – Textural properties of the La_2O_3 support and fresh 20wt%Co/80wt%La_2O_3 catalyst.

Textural properties	La_2O_3	20wt%Co/80wt%La_2O_3
Specific Surface area ($m^2\ g^{-1}$)	8.33	16.45
Cumulative pore area ($m^2\ g^{-1}$)	7.34	15.13
Cumulative pore volume ($m^3\ g^{-1}$)	0.0113	0.0289
Average pore diameter (nm)	1.14	1.22

(averaged 200 nm) that appear fused, most likely resulting from the high calcination temperature employed during the catalyst synthesis. Significantly, the EDX analysis in Fig. 4 reveals the presence of Co, La and O in the as-prepared catalyst, hence consistent with the XRD diffraction pattern. The stipulated amount of the elemental compositions of the as-prepared catalyst (20wt%Co/80wt%La_2O_3), from analyses carried out at five different spots and averaged, was consistent with the values of 18wt%Co and 82wt%La_2O_3 obtained from the EDX dot analysis (refers to Fig. 4).

The textural properties of the bare La_2O_3 support, as well as the 20wt%Co/80wt%La_2O_3 catalyst are shown in Table 1. The BET specific surface area obtained for the La_2O_3 support was found to be 8.33 $m^2\ g^{-1}$ with corresponding cumulative pore area and pore volume of 7.34 $m^2\ g^{-1}$, and 0.0113 $m^3\ g^{-1}$ respectively. Interestingly, the values of the BET specific surface area, the cumulative pore area and pore volume were found to increase to 16.45 $m^2\ g^{-1}$, 15.13 $m^2\ g^{-1}$ and 0.0289 $m^3\ g^{-1}$ respectively, when 20wt% Co metal was formulated into the matrix of support. The low BET specific surface area of the pristine La_2O_3 support demonstrates that the surface was less porous, and that the deposition of cobalt metal has primarily occurred on the surface of the La_2O_3 support. This Co deposit yielded a rougher and bulkier surface area for the resultant 20wt%Co/80wt%La_2O_3 catalyst; hence the improved textural properties. This observation is also consistent with the findings of Rahemi et al. [30] who reported an increment in the textural properties of γ-Al_2O_3 by the dispersion of Ni and Co-metals. The BET specific surface area obtained for the Co/La_2O_3 catalyst is comparable with 16.60 $m^2\ g^{-1}$ obtained by Perefiguez et al. [31] for Ni/La_2O_3 catalyst. The N_2-adsorption-desorption isotherm of the Co/La_2O_3 catalyst is depicted in Fig. 5. It can be seen that the adsorption and desorption of liquid N_2 on the Co/La_2O_3 catalyst exhibits Type IV isotherm with H1 hysteresis according to IUPAC classification. This implies that the Co/La_2O_3 is of mesoporous textural property with narrow distribution of uniform mesopores with cylindrical-like pore geometric.

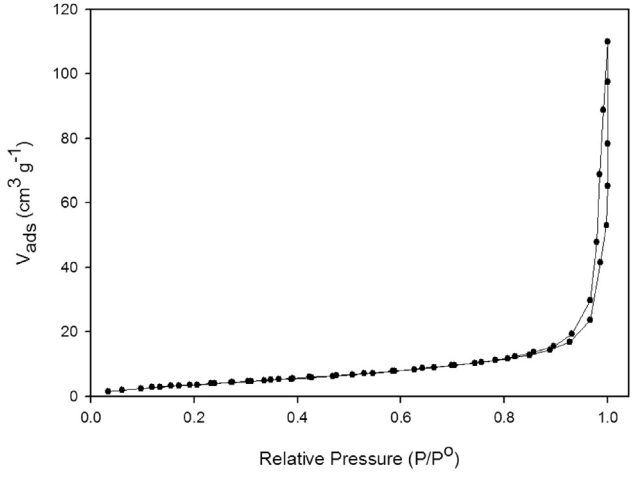

Fig. 5 – N_2 adsorption-desorption isotherm of the fresh 20wt%Co/80wt%La_2O_3 catalyst.

Thermogravimetric analysis of the uncalcine catalyst

The thermogravimetry (TG) and differential thermogravimetry (DTG) profiles of the as-prepared catalyst showing the variation of the weight loss and derivative weight loss of the catalyst with respect to changes in temperature are depicted in Fig. 6. Significantly, the TG and DTG profiles show five main peaks (I–V) signifying the sequential weight losses of physical and hydrated water, decomposition of metal nitrates and subsequent oxidation of the resultant oxides (cf. Eqs. (7)–(10)). Peaks I–III formed at 318 K, 340 K and 393 K, respectively, may be associated with the sequential loss of hydrated water, while peaks IV and V formed at 518 K and 564 K, respectively, can be attributed to the decomposition of metal nitrate [32]. Interestingly, no other peak was formed beyond 610 K which signifies the thermal stability of the Co oxides. Hence, the calcination temperature of the dried, fresh catalyst was fixed at 873 K for the reaction studies.

$$Co(NO_3)_2\cdot 6H_2O \rightarrow Co(NO_3)_2\cdot 4H_2O + 2H_2O \quad (7)$$

$$Co(NO_3)_2\cdot 4H_2O \rightarrow Co(NO_3)_2\cdot 2H_2O + 2H_2O \quad (8)$$

$$Co(NO_3)_2\cdot 2H_2O \rightarrow Co(NO_3)_2 + 2H_2O \quad (9)$$

$$Co(NO_3)_2 \rightarrow CoO + 2NO_2 + {}^1/_2O_2 \quad (10)$$

Furthermore, the solid state kinetics parameters (A and E_a) were obtained from the Kissinger and Ozawa-Flynn-Wall kinetics plots shown in Fig. 6. The kinetics parameters as well as the coefficient of determination (R^2) obtained from both the Kissinger and Ozawa-Flynn-Wall models are summarized in

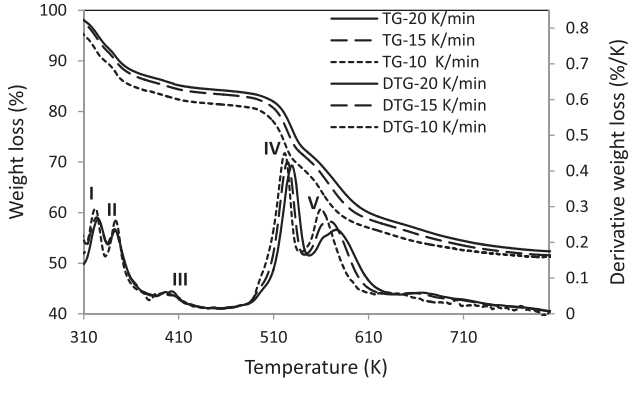

Fig. 6 – TG and DTG representing calcination curves of the dried, fresh 20wt%Co/80wt%La_2O_3 catalyst.

Table 2. Peaks I–III are model-fittings within temperature range of 310–410 K at different heating rates, while peaks IV–V are model-fittings at temperature ranged 510–620 K, also at different heating rates. Significantly, the non-isothermal apparent activation energy values of 133.84, 382.48 and 221.65 kJ mol^{-1} were obtained for peaks I–III, respectively. The high apparent activations values obtained for peaks I–III could be attributed to different bond characteristics associated with the loss of hydrated water [33]. The values of the apparent activation energy values obtained for the loss of hydrated water was consistent with that reported by Ihli et al. [33] at temperatures range of 313–500 K. Interestingly, the apparent energy values of 143.16, 391.14 and 229.01 kJ mol^{-1} obtained for peaks I–III using the Ozawa-Flynn-Wall kinetics are not at much variance with that obtained from the Kissinger kinetics model. The high $R^2 > 0.95$ and low standard error of estimates (SEE) obtained for model fittings in both the Kissinger and Ozawa-Flynn-Wall kinetics models indicate good fittings of the data. Moreover, apparent activation energy of 162.87 and 142.25 kJ mol^{-1} were obtained for peaks IV and V from the Kissinger model which was nearly identical with 168.56 and 147.57 kJ mol^{-1} obtained for the same peaks from the Ozawa-Flynn-Wall kinetics model. The high apparent activation energies obtained for the decomposition of the metal nitrates during the calcination process is typical of non-catalyzed gas–solid reaction controlled system [34].

Catalytic testing

The catalytic performance of the 20%Co/80%La_2O_3 as a function of the reactant (CH_4 and CO_2) conversions as well as the products (H_2 and CO) at reaction temperature ranged 923–1023 K and feed ratios ranged 0.1–1.0 are depicted in Fig. 7. Significantly, both the CH_4 and CO_2 conversions as well as the H_2 and CO yields increase with feed ratios and reaction temperature. There was an increases in CH_4 conversion from 2% (feed ratio of 0.1 and reaction temperature of 923 K) and reached the maximum value of ca.50% (feed ratio of 1.0 and reaction temperature of 1023 K). Interestingly, the catalysts showed a higher conversion of CO_2 than CH_4. The CO_2 conversion increases 2% (feed ratio of 0.1 and reaction temperature of 923 K) to ca.60% (feed ratio of 1.0 and reaction temperature of 1023 K). This trend could be as a result of the occurrence of side reaction such as reverse water gas shift reaction which favors the production of more CO from partly consumed H_2. The highest values of CH_4 and CO_2 conversion obtained in this study is slightly lower than that obtained by Sutthiumporn and Kawi [31] who obtained highest CH_4 and CO_2 conversions of ca.65% and 49% respectively over Ni/La_2O_3 catalyst. The difference in the CH_4 and CO_2 conversions could be attributed to the Co and Ni activities over the La_2O_3 support. Furthermore, the catalysts showed an increasing trend in activity in terms of H_2 and CO yields. The Co/La_2O_3 catalyst gave the highest yield of ca.40% and ca.56% for H_2 and CO respectively. Surprisingly, the H_2 yield obtained in this study is higher than that obtained by Sutthiumporn and Kawi [31] (ca.35%)

Kinetics studies

Effects of partial pressure on the CH_4 and CO_2 consumption rates

The effects of partial pressure on the rates of consumption of CH_4 and CO_2 at 923, 973 and 1023 K are depicted in Fig. 8. The kinetics measurements were performed below and above stoichiometric ratio (CO_2:CH_4). The kinetics measurements below stoichiometric was investigated by varying the partial pressure of CH_4 from 5 to 50 kPa at constant CO_2 partial pressure (50 kPa). Moreover, the kinetics measurements were also performed when both CH_4 and CO_2 partial pressure equal to 50 kPa. Furthermore, the kinetics measurements for the above stoichiometric ratios were performed by keeping the partial pressure of CH_4 constant (50 kPa) while varying the partial pressure of CO_2 between 5 and 50 kPa. The analysis of the kinetics data showed that at below and above stoichiometric ratio, the rates of consumptions of the CH_4 and CO_2 were sensitive to changes in the partial pressures and temperature. It is noteworthy that the rates of consumption of both CH_4 and CO_2 increased non-linearly with partial pressures and reaction temperatures. Interestingly, higher rates of CO_2 consumption were obtained below stoichiometric compared to rates of CH_4 consumption. This could be attributed to the affinity of the CO_2 to the basic site of the catalyst as reported by Sato et al. [17]. Similarly, higher rates of CH_4 consumption was favored at conditions above stoichiometric compared to rate of CO_2 consumption (cf. Fig. 8(b) and (d)). This could be as a result of strong influence of methane

Table 2 – Kinetics parameters of the temperature programmed calcination of the fresh, dried catalyst.

Parameters	I	II	III	IV	V
Kissinger kinetics model					
E_a (kJ mol^{-1})	133.84	382.48	221.65	162.87	142.25
A	2.02×10^{12}	5.41×10^{38}	2.9×10^{29}	1.82×10^{25}	4.00×10^{24}
R^2	0.96	0.99	0.99	0.99	0.99
[a]SEE	0.092	0.047	0.047	0.047	0.046
Ozawa-Flynn-Wall kinetics model					
E_a (kJ mol^{-1})	143.16	391.14	229.01	168.56	147.57
A	3.48×10^{12}	1.05×10^{38}	9.83×10^{28}	8.18×10^{24}	2.05×10^{23}
R^2	0.96	0.99	0.99	0.99	0.99
[a]SEE	0.092	0.047	0.047	0.046	0.046

[a] SEE = Standard Error of Estimate.

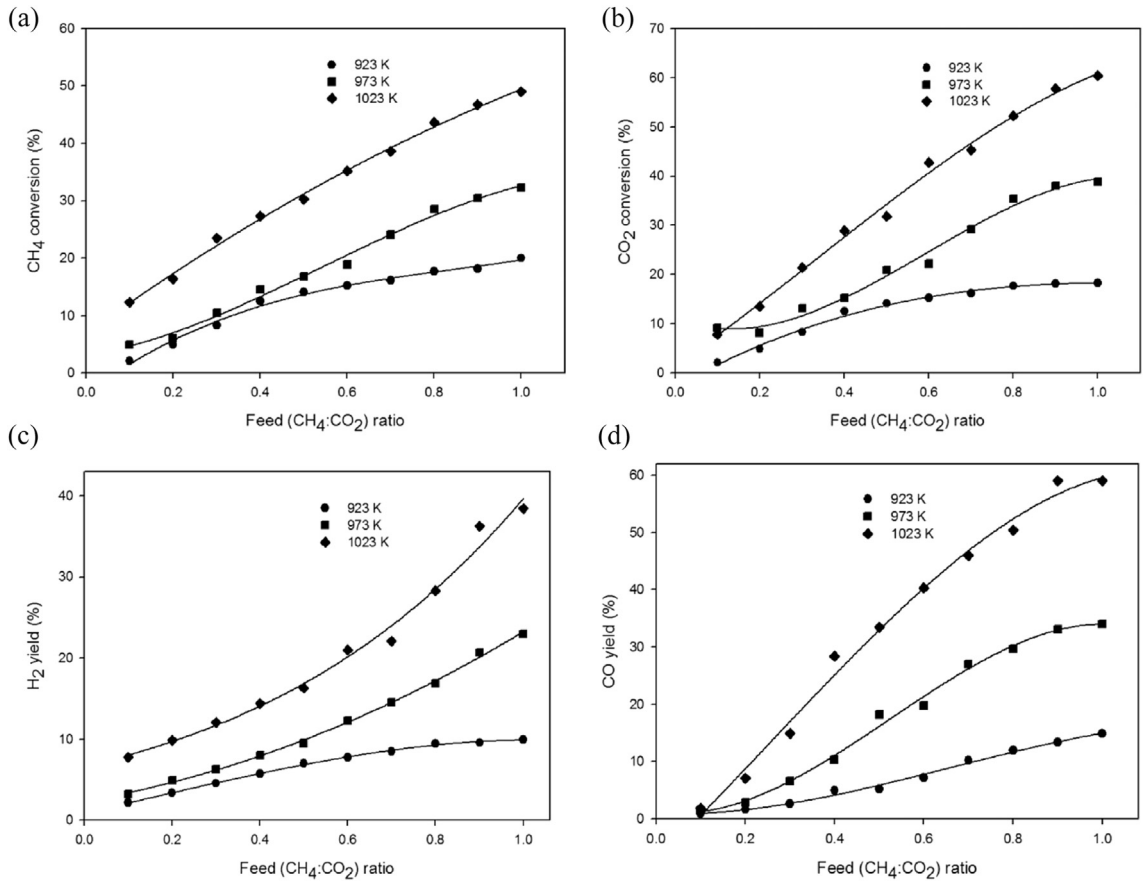

Fig. 7 – Effects of reactant feed ratio (CH_4:CO_2) on (a) conversion of CH_4 (b) conversion CO_2 (c) H_2 yield and (d) CO yield at 923, 973 and 1023 K.

cracking on the dry reforming reaction performed above stoichiometric [1]. Comparison of Fig. 8(a) and (b) showed that the rate of consumption of CH_4 was more influenced by the increase in CO_2 partial pressure than that of CH_4. This trend could be due to stronger adsorption of CO_2 onto the 20wt%Co/80wt%La_2O_3 catalyst compared to CH_4. Similar observation has been reported by Gallego et al. [35] for Ni/La_2O_3 catalyst. Indeed, La_2O_3 was employed as a material for storing CO_2 adsorbate as reported by previous work [17].

Effects of partial pressure on the rate of formation of H_2 and CO

The rates of formation of H_2, as well as that of CO with respect to changes in partial pressures of reactants and temperature ranged 923–1023 K were also computed and shown in Fig. 9. Generally, the rates of formation of H_2 and CO increased with partial pressure and temperature, consistent with trends observed in Fig. 7. Nevertheless, a higher rate of formation of CO was observed with CH_4 partial pressure at conditions below stoichiometric compared to a lower rate of H_2 (cf. Fig. 9 (a) and (c)). This could be attributed to the influence of parallel reactions such as reverse Boudouard and water gas shift reactions on the formation of products. Furthermore, at conditions above stoichiometric, higher rate of formation of H_2 was observed compared to the rate of formation of CO (cf. Fig. 9 (b) and (d)). The rate of CO formation could have been impaired as a result of reduction of CO formed by H_2 which often leads to formation of carbon and water [1]. Moreover, the higher rates of H_2 formation obtained with partial pressure of CO_2 could be attributed to strong influence of methane cracking which yield carbon and H_2.

Power law kinetics modeling

The data obtained from the kinetics measurements were first fitted into a simple power-law model represented in Eq. (11) in order to mathematically-capture the consumption rates of CH_4 and CO_2, as well as formation rates of H_2 and CO. Levenberg–Marquardt algorithm was employed to evaluate the kinetics parameters from the non-linear power-law model using Polymath version 6.1 software.

$$r_i = A\exp\left(\frac{-E_a}{RT}\right)P_{CH_4}^{\alpha}P_{CO_2}^{\beta} \tag{11}$$

where r_i is rates of consumption of CH_4 and CO_2, as well as rates of formation of H_2 and CO; α and β are reaction orders with respect to the desired species; A is the pre-exponential factor; E_a is the apparent activation energy; R is the universal gas constant; T is the reaction temperature in absolute term while P_{CH_4} and P_{CO_2} are the partial pressure of CH_4 and CO_2, respectively.

The values of the kinetics parameters, as well as the corresponding R^2 are summarized in Table 3. The apparent

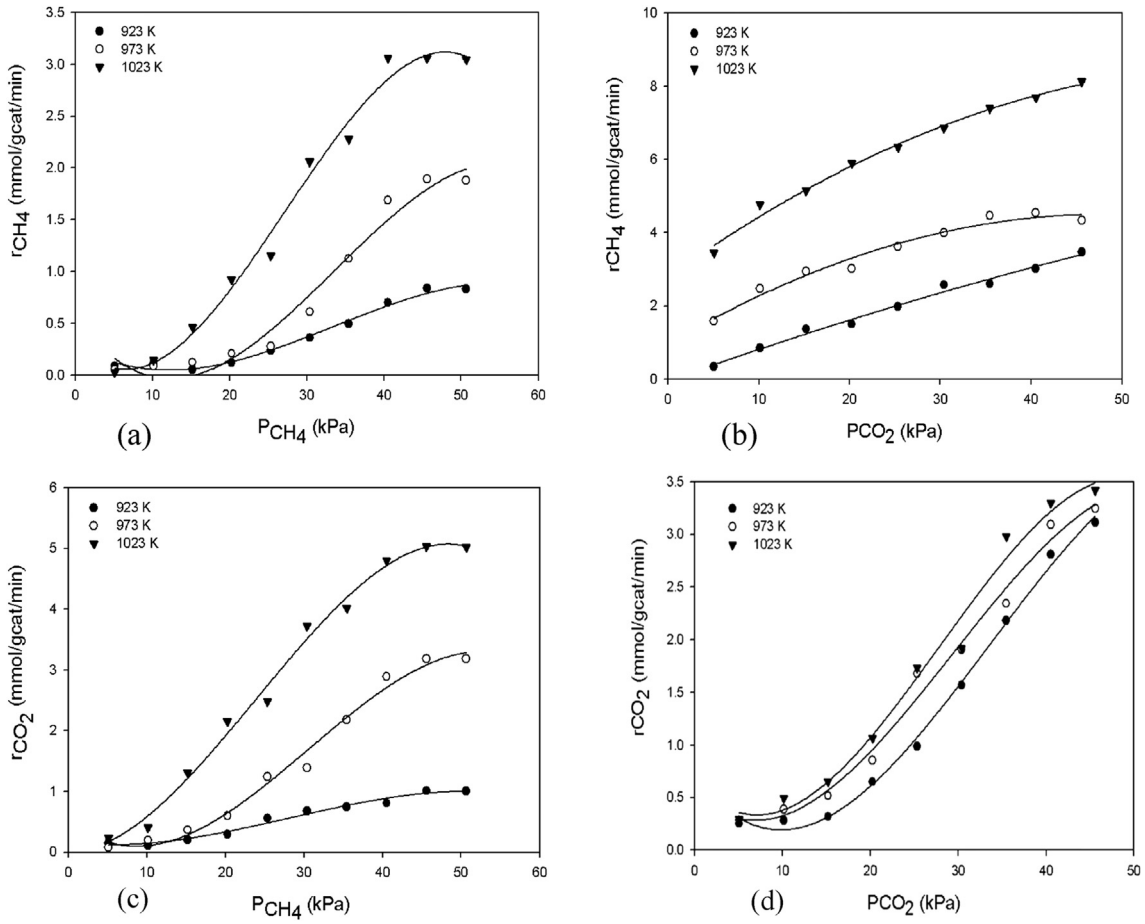

Fig. 8 – Effects of reactant partial pressure on the rate of consumptions of CH_4 and CO_2 at 923, 973 and 1023 K.

activation energy of 96.46 and 72.22 kJ mol^{-1} obtained for the consumptions of CH_4 and CO_2, respectively, are nearly identical with the reported values (E_{CH_4} = 96.30 and 92.1 kJ mol^{-1}; E_{CO_2} = 79.6 and 87.9 kJ mol^{-1}) by Bradford et al. [36] for kinetics study of methane dry forming over Ni/SiO_2 and Ni/MgO catalysts at temperatures that ranged 673–823 K. The higher activation energy for the CH_4 species compared to CO_2 indicates that the consumption rate of CH_4 was more sensitive to the changes in reaction temperature. However, the values of apparent activation energy values obtained in this study were found to be lower than the values of 100.56 and 106.84 kJ mol^{-1} reported by Wei et al. [37] and Cui et al. [38] using Pt/ZrO_2 and Ni/α-Al_2O_3 catalysts. Significantly, this indicates that lanthanum supported cobalt catalyst exhibits superior catalytic performance compared to its nickel counterpart. This may be due to high oxygen storing capacity of the La_2O_3 support which provides lattice oxygen for the gasification of carbon deposited on the surface of the catalyst; hence its improved activity. In addition, the activation energy of 101.5 kJ mol^{-1} obtained for the formation of H_2 was higher than the formation of CO by a margin of 31.79 kJ mol^{-1}. Significantly, the activation energy of CH_4 (96.44 kJ mol^{-1}) was quite close to the H_2 formation (101.5 kJ mol^{-1}), whilst activation energy of CO_2 (72.22 kJ mol^{-1}) was comparable to the CO (69.71 kJ mol^{-1}). Based on these activation energy trends, we posit that during methane dry reforming over the 20wt% Co/80wt%La_2O_3 catalyst, the plausible reaction steps would primarily involve CH_4 decomposition into solid carbon (C) and H_2 ($CH_4 \rightarrow C + 2H_2$). Subsequently, the C would partake in the reverse-Boudouard reaction to produce CO ($C + CO_2 \rightarrow CO$).

The parity plots of the predicted rate values for consumptions of CH_4 and CO as well as the formation of H_2 and CO from the power-law model and the experimental rate values are depicted in Fig. 10. It can be seen that the predicted rates from the power-law and the experimental rate values are in good agreement.

Mechanistic study of the methane dry reforming over 20wt%Co/80wt%La_2O_3

Methane and CO_2 adsorption on the surface of the 20wt%Co/80wt%La_2O_3 catalyst could either be on a similar site or individual adsorption on separate site. Several authors have reported dual site CH_4 and CO_2 adsorption mechanisms for methane dry reforming [21,39–41]. Therefore, in the present study, both single- and dual-site Langmuir–Hinshelwood mechanisms for the methane dry reforming were considered.

The single site mechanism for methane dry reforming assumes that only the site in which the CH_4 and CO_2 are adsorbed take part in the reaction. Tsipouriari et al. [42] and Moradi et al. [43] in their reports have proposed 2 step-single site rate determining step (RDS) as shown in Eqs. (12)–(15)

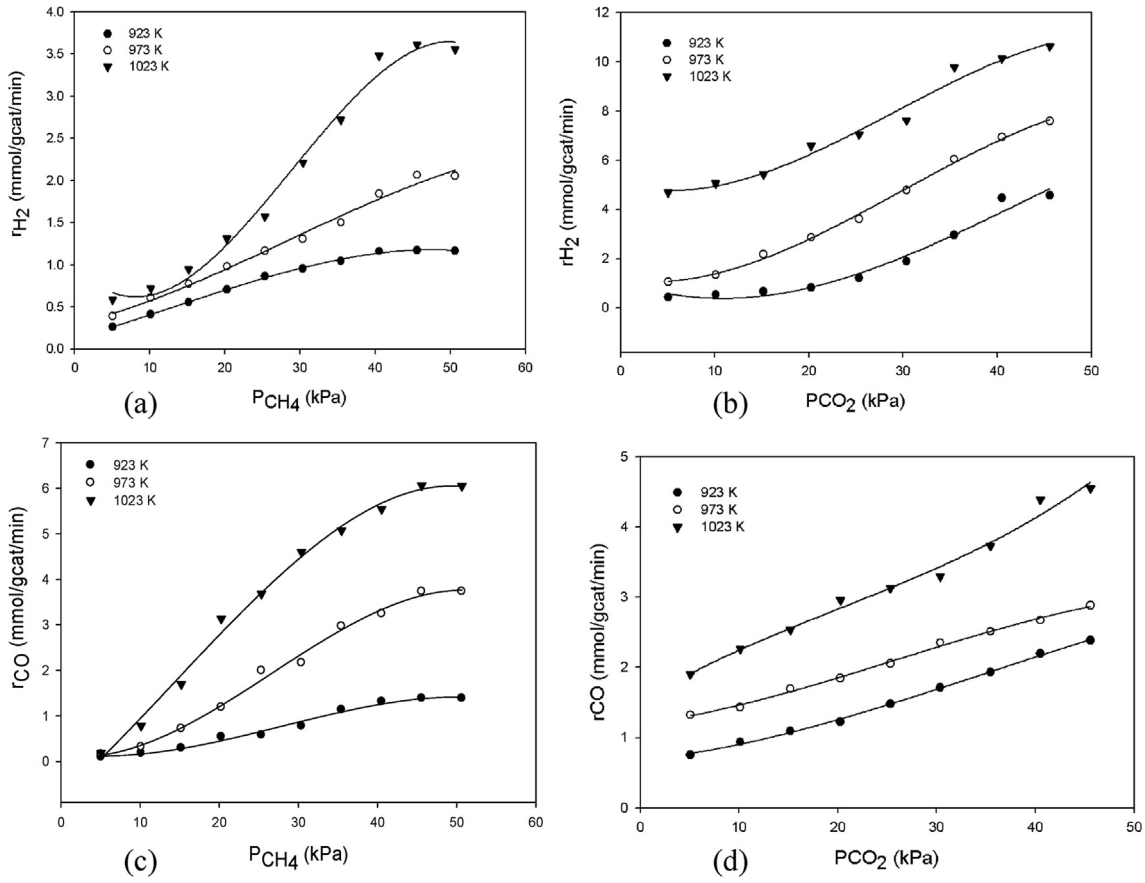

Fig. 9 – Effect of reactant partial pressure on the rate of formation of H_2 and CO at 923, 973 and 1023 K.

$$CH_4 + \theta \rightleftharpoons CH_4 - \theta \quad \text{equilibrium} \tag{12}$$

$$CH_4 - \theta \rightleftharpoons C_s - \theta + 2H_2\uparrow \quad \text{RDS} \tag{13}$$

$$CO_2 + La_2O_3 \rightleftharpoons La_2O_2CO_3 \quad \text{equilibrium} \tag{14}$$

$$La_2O_2CO_3 + C_s - \theta \rightarrow La_2O_3 + 2CO\uparrow + \theta \quad \text{RDS} \tag{15}$$

In the dual-site mechanism, CH_4 and CO_2 are preferentially adsorbed on two non-identical sites available on catalyst surface. The dual-site mechanism has been reported by Pichas et al. [39] for kinetics of methane dry reforming over $La_{2-x}Sr_xNiO_4$ perovskite-type oxides catalyst as shown in Eqs. (16)–(18).

$$CH_4 + \theta \rightleftharpoons CH_4 - \theta \quad \text{equilibrium} \tag{16}$$

Table 3 – Estimation of kinetics parameters from the power-law model.

Reaction species	Kinetics parameters					
	α	β	A(mmol min^{-1} $kPa^{-(\alpha+\beta)}$)	E_a (kJ mol^{-1})	R^2	[a]Rmsd
CH_4	3.66	0.35	0.1	96.44	0.95	0.09
CO_2	1.20	1.30	1.3	72.22	0.89	0.06
H_2	3.84	0.47	0.072	101.5	0.88	0.2
CO	0.93	0.68	36.34	69.71	0.88	0.07

[a] Rmsd = Root mean square deviation.

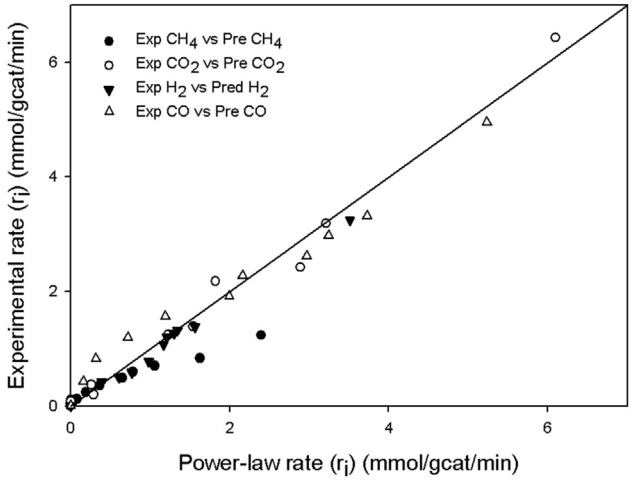

Fig. 10 – Parity plots for the reaction rates by the power-law model.

$$CO_2 + \beta \rightleftharpoons CO_2 - \beta \quad \text{equilibrium} \tag{17}$$

$$CH_4 - \theta + CO_2 - \beta \rightarrow 2H_2\uparrow + 2CO\uparrow + \theta + \beta \quad \text{RDS} \tag{18}$$

Based on the different mechanisms of methane dry reforming over La_2O_3 supported metal catalysts proposed in the literature, the kinetics data obtained from this study were tested in the Langmuir–Hinshelwood rate expressions summarized in Table 4.

The summary of the kinetics parameters estimated from each of the Langmuir–Hinshelwood non-linear regression rate expressions are summarized in Table 5. The coefficient of determination (R^2) obtained from fitting the experimental data into the six models reveal that all the models have R^2 values $\geq$ 0.9 except Models 5 and 6 which have R^2 values < 0.9. Hence, these two models were excluded from the best options. Furthermore, estimated values of K_{CH_4} and K_{CO_2} for Models 3 and 4 remain constant after 923 K, hence did not show obvious sensitivity to changes in temperature, in violation of thermodynamics aspect. Consequently, Models 3 and 4 were also excluded leaving out only Models 1 and 2. Models 1 and 2 were further screened using criteria defined in Eqs. (19) and (20).

$$10 \leq -\Delta S_{exp} \text{ and } -\Delta S_{exp} \leq 12.2 - 0.0014\,\Delta H_{exp} \tag{19}$$

where $-\Delta S_{exp}$ is the experimental adsorption entropy and $-\Delta H_{exp}$ is the experimental adsorption enthalpy which can be estimated from Eq. (15).

$$lnK = -\frac{\Delta H_{exp}}{RT} + \frac{\Delta S_{exp}}{R} \tag{20}$$

The estimates of ΔS_{exp} and ΔH_{exp} obtained for Models 1 and 2 (refer to Table 6) showed that both models satisfied the conditions in Eq. (16). However, R^2 values of 0.9979 and 0.9395 obtained for Model 2 is far higher compared to 0.1934 and 0.0978 obtained for Model 1. Hence, Model 2 emerged as the best Langmuir–Hinshelwood kinetics model, representing mechanisms of the methane dry reforming over 20wt%Co/80wt%La_2O_3 catalyst in the current work.

Interestingly, the activation energy of 98.17 kJ mol^{-1} obtained from Fig. 11 based on the rate constants obtained from the Model 2 does not show much variance from that obtained from the power-law model. Based on the kinetics parameters obtained from Model 2, we herein propose that the mechanisms of the methane dry reforming over 20wt%Co/80wt%La_2O_3 catalyst follows dual site associative adsorption of both CH_4 and CO_2 with bimolecular surface reaction. In order to further investigate the appropriateness of the dual-site Langmuir–Hinshelwood kinetics model adopted to describe the mechanism of the methane dry reforming reaction over 20wt%Co/80wt%La_2O_3 catalyst, parity plot showing the comparing between the experimental rate of CH_4 consumption and the predicted Langmuir–Hinshelwood rate of CH_4 consumption is depicted in Fig. 12. It is worthwhile knowing that the experimental rate of CH_4 consumption and the predicted Langmuir–Hinshelwood rate of CH_4 consumption are in good agreement.

Conclusions

The production of CO-rich hydrogen from methane dry reforming as well as the kinetics and mechanism were studied extensively over a 20wt%Co/80wt%La_2O_3 catalyst from 923 to 1023 K, feed ratio ranged 0.1–1.0. and partial pressure ranged 10–50 kPa. The catalytic activity test shows that highest CH_4 and CO_2 conversion of 50% and 60% with corresponding H_2 and CO yield of 45% and 58% respectively were obtained. The mechanism and Langmuir–Hinshelwood kinetics expression for the methane dry reforming over the Co/La_2O_3 catalyst were derived considering single-and dual-site adsorption mode. The different models obtained were statistically and thermodynamically discriminated to obtain the model that best describe the experimental data. The analysis of the experimental data fitted into the power-law rate expressions and Langmuir–Hinshelwood kinetics model yielded activation energy values of 96.11 and 98.44 kJ mol^{-1}, respectively. A lower activation energy *ca.* 72 kJ mol^{-1} was obtained for consumption of CO_2 which signifies that reaction rate of CO_2 proceeds faster compared to that of CH_4. The interpretation of the Langmuir–Hinshelwood kinetics model from the experimental data showed that mechanism of the methane dry reforming reaction can be described by dual-site molecular adsorption of both CH_4 and CO_2 on non-identical site with surface reaction as the rate determining step.

Table 4 – Proposed Langmuir–Hinshelwood rate expressions for methane dry reforming.

No	Model	Description	Reference
1	$\frac{k_{rxn}P_{CH_4}P_{CO_2}}{(1+K_{CH_4}P_{CH_4}+K_{CO_2}P_{CO_2})^2}$	Molecular adsorption of both CH_4 and CO_2 on the single site with bimolecular surface reaction.	[44,45]
2	$\frac{k_{rxn}P_{CH_4}P_{CO_2}}{(1+K_{CH_4}P_{CH_4})(1+K_{CO_2}P_{CO_2})}$	Dual site associative adsorption of both CH_4 and CO_2 with bimolecular surface reaction.	[39]
3	$\frac{k_{rxn}P_{CH_4}\sqrt{P_{CO_2}}}{(1+K_{CH_4}P_{CH_4}+\sqrt{K_{CO_2}P_{CO_2}})^2}$	Single site associative adsorption of CH_4 and dissociative adsorption of CO_2 with bimolecular surface reaction	[32]
4	$\frac{k_{rxn}P_{CO_2}\sqrt{P_{CH_4}}}{(1+\sqrt{K_{CH_4}P_{CH_4}})(1+K_{CO_2}P_{CO_2})}$	Dual site associative adsorption of CO_2 and dissociative adsorption of CH_4 with bimolecular surface reaction	[32]
5	$\frac{k_{rxn}\sqrt{P_{CH_4}P_{CO_2}}}{(1+\sqrt{K_{CH_4}P_{CH_4}}+\sqrt{K_{CO_2}P_{CO_2}})^2}$	Single site dissociative adsorption of both CH_4 and CO_2 with bimolecular surface reaction.	[46]
6	$\frac{k_{rxn}\sqrt{P_{CH_4}P_{CO_2}}}{(1+\sqrt{K_{CO_2}P_{CO_2}})(1+\sqrt{K_{CH_4}P_{CH_4}})}$	Dual site dissociative adsorption of both $_{CH4}$ and CO_2 with bimolecular surface reaction.	[34]

Table 5 – Kinetics parameters estimated from the Langmuir–Hinshelwood models.

Model	Temperature (K)	k_{rxn} (mmol min^{-1} $kPa^{-(\alpha+\beta)}$)	K_{CH_4}	K_{CO_2}	R^2	Rmsd
1	923	1.6×10^{-4}	0.015	0.002	0.90	0.12
	973	7.8×10^{-4}	0.013	0.008	0.92	0.14
	1023	2.0×10^{-3}	0.017	0.003	0.96	0.17
2	923	2.7×10^{-3}	0.019	0.014	0.99	0.03
	973	4.2×10^{-3}	0.018	0.013	0.98	0.07
	1023	9.5×10^{-3}	0.017	0.011	0.95	0.19
3	923	2.2×10^{-3}	0.015	0.003	0.93	0.1
	973	2.2×10^{-3}	0.017	0.005	0.98	0.06
	1023	4.1×10^{-4}	0.017	0.005	0.96	0.17
4	923	2.2×10^{-4}	0.077	0.0004	0.99	0.04
	973	7.0×10^{-4}	0.077	0.003	0.99	0.05
	1023	1.3×10^{-3}	0.077	0.003	0.98	0.12
5	923	5.70×10^{-5}	0.021	0.41	0.74	0.18
	973	1.7×10^{-4}	0.0043	0.63	0.87	0.17
	1023	7.70×10^{-5}	0.023	0.32	0.88	0.3
6	923	8.99×10^{-8}	0.038	0.028	0.96	0.07
	973	6.62×10^{-7}	0.032	0.033	0.86	0.19
	1023	9.81×10^{-7}	0.033	0.033	0.79	0.39

Table 6 – Parameter estimates for discrimination of Models 1 and 2.

Parameter	Model no	Value	R^2
ΔS_{CH_4} (J mol^{-1} K^{-1})	1	0.0022	0.1934
	2	−0.0061	0.9979
ΔH_{CH_4} (kJ mol^{-1})	1	9.26	0.1934
	2	8.72	0.9979
ΔS_{CO_2} (J mol^{-1} K^{-1})	1	0.28	0.0978
	2	−0.0012	0.9395
ΔH_{CO_2} (J mol^{-1})	1	3.49	0.0978
	2	1.88	0.9395

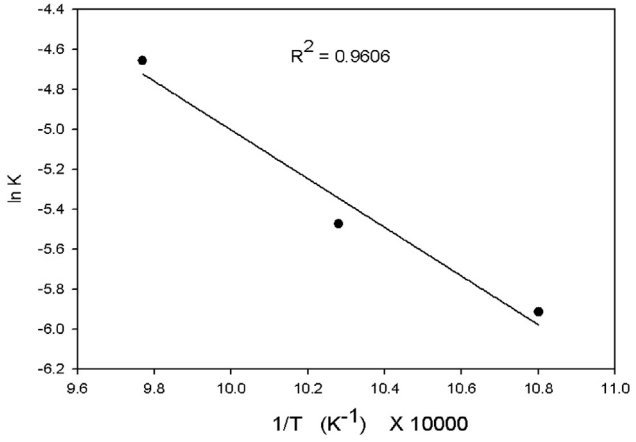

Fig. 11 – Estimation of activation energy from Model 2.

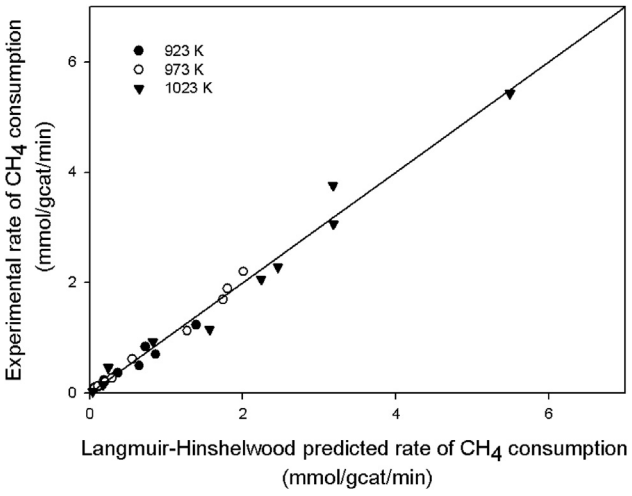

Fig. 12 – Parity plot for the rate of consumption of CH_4 by Langmuir–Hinshelwood kinetics model.

Acknowledgments

The authors would like to acknowledge the Science fund RDU130501 granted by the Ministry of Science, Technology and Innovation Malaysia (MOSTI) and the DSS scholarship awarded to B.V. Ayodele by the Universiti Malaysia Pahang.

REFERENCES

[1] Lavoie J-M. Review on dry reforming of methane, a potentially more environmentally-friendly approach to the increasing natural gas exploitation. Front Chem 2014;2:1–17. http://dx.doi.org/10.3389/fchem.2014.00081.

[2] Sajjadi SM, Haghighi M, Rahmani F. Dry reforming of greenhouse gases CH_4/CO_2 over MgO-promoted Ni-Co/Al_2O_3-ZrO_2 nanocatalyst: effect of MgO addition via sol-gel method on catalytic properties and hydrogen yield. J Sol-Gel Sci Technol 2014:1–14. http://dx.doi.org/10.1007/s10971-014-3280-1.

[3] Ayodele BV, Khan MR, Cheng CK. Syngas production from CO_2 reforming of methane over ceria supported cobalt catalyst: effects of reactants partial pressure. J Nat Gas Sci Eng 2015. http://dx.doi.org/10.1016/j.jngse.2015.09.049.

[4] Holladay JD, Hu J, King DL, Wang Y. An overview of hydrogen production technologies. Catal Today 2009;139:244–60. http://dx.doi.org/10.1016/j.cattod.2008.08.039.

[5] Gangadharan P, Kanchi KC, Lou HH. Evaluation of the economic and environmental impact of combining dry reforming with steam reforming of methane. Chem Eng Res Des 2012;90:1956–68. http://dx.doi.org/10.1016/j.cherd.2012.04.008.

[6] Vita A, Cristiano G, Italiano C, Pino L, Specchia S. Syngas production by methane oxy-steam reforming on Me/CeO2 (Me=Rh, Pt, Ni) catalyst lined on cordierite monoliths. Appl Catal B Environ 2015;162:551–63. http://dx.doi.org/10.1016/j.apcatb.2014.07.028.

[7] Budiman AW, Song S-H, Chang T-S, Shin C-H, Choi M-J. Dry reforming of methane over cobalt catalysts: a literature review of catalyst development. Catal Surv Asia 2012;16:183–97. http://dx.doi.org/10.1007/s10563-012-9143-2.

[8] Alenazey FS. Utilizing carbon dioxide as a regenerative agent in methane dry reforming to improve hydrogen production and catalyst activity and longevity. Int J Hydrogen Energy 2014;39:18632–41. http://dx.doi.org/10.1016/j.ijhydene.2014.02.148.

[9] Xiong H, Moyo M, Motchelaho MA, Tetana ZN, Dube SM, Jewell LL, et al. Fischer-Tropsch synthesis: iron catalysts supported on N-doped carbon spheres prepared by chemical vapor deposition and hydrothermal approaches. J Catal 2014;311:80–7. http://dx.doi.org/10.1016/j.jcat.2013.11.007.

[10] Yao Y, Liu X, Hildebrandt D, Glasser D. Fischer-Tropsch synthesis using $H_2/CO/CO_2$ syngas mixtures over an iron catalyst. Ind Eng Chem Res 2011;50:11002–12. http://pubs.acs.org/doi/pdf/10.1021/ie200690y.

[11] Lee J-H, You Y-W, Ahn H-C, Hong J-S, Kim S-B, Chang T-S, et al. The deactivation study of Co–Ru–Zr catalyst depending on supports in the dry reforming of carbon dioxide. J Ind Eng Chem 2014;20:284–9. http://dx.doi.org/10.1016/j.jiec.2013.03.036.

[12] Wang C, Sun N, Zhao N, Wei W, Sun Y, Sun C, et al. Coking and deactivation of a mesoporous Ni–CaO–ZrO_2 catalyst in dry reforming of methane: a study under different feeding compositions. Fuel 2015;143:527–35.

[13] Pakhare D, Spivey J. A review of dry (CO_2) reforming of methane over noble metal catalysts. Chem Soc Rev 2014;43. http://dx.doi.org/10.1039/c3cs60395d.

[14] Laosiripojana N, Sutthisripok W, Assabumrungrat S. Synthesis gas production from dry reforming of methane over CeO_2 doped Ni/Al_2O_3: influence of the doping ceria on the resistance toward carbon formation. Chem Eng J 2005;112:13–22. http://dx.doi.org/10.1016/j.cej.2005.06.003.

[15] Kambolis A, Matralis H, Trovarelli A, Papadopoulou C. Ni/CeO_2-ZrO_2 catalysts for the dry reforming of methane. Appl Catal A Gen 2010;377:16–26. http://dx.doi.org/10.1016/j.apcata.2010.01.013.

[16] Yu X, Wang N, Chu W, Liu M. Carbon dioxide reforming of methane for syngas production over La-promoted NiMgAl catalysts derived from hydrotalcites. Chem Eng J 2012;209:623–32. http://dx.doi.org/10.1016/j.cej.2012.08.037.

[17] Sato S, Takahashi R, Kobune M, Gotoh H. Basic properties of rare earth oxides. Appl Catal A Gen 2009;356:57–63. http://dx.doi.org/10.1016/j.apcata.2008.12.019.

[18] Mattos LV, Rodino E, Resasco DE, Passos FB, Noronha FB. Partial oxidation and CO_2 reforming of methane on Pt/Al_2O_3, Pt/ZrO_2, and Pt/Ce-ZrO_2 catalysts. Fuel Process Technol 2003;83:147–61. http://dx.doi.org/10.1016/S0378-3820(03)00063-8.

[19] Sadykov VA, Gubanova EL, Sazonova NN, Pokrovskaya SA, Chumakova NA, Mezentseva NV, et al. Dry reforming of methane over Pt/PrCeZrO catalyst: kinetic and mechanistic features by transient studies and their modeling. Catal Today 2011;171:140–9. http://dx.doi.org/10.1016/j.cattod.2011.04.004.

[20] Munera J, Irusta S, Cornaglia L, Lombardo E, Vargascesar D, Schmal M. Kinetics and reaction pathway of the CO_2 reforming of methane on Rh supported on lanthanum-based solid. J Catal 2007;245:25–34. http://dx.doi.org/10.1016/j.jcat.2006.09.008.

[21] Pakhare D, Schwartz V, Abdelsayed V, Haynes D, Shekhawat D, Poston J, et al. Kinetic and mechanistic study of dry (CO_2) reforming of methane over Rh-substituted $La_2Zr_2O_7$ pyrochlores. J Catal 2014;316:78–92. http://dx.doi.org/10.1016/j.jcat.2014.04.023.

[22] Verykios XE. Catalytic dry reforming of natural gas for the production of chemicals and hydrogen. Int J Hydrogen Energy 2003;28:1045–63. http://dx.doi.org/10.1016/S0360-3199(02)00215-X.

[23] Kathiraser Y, Oemar U, Saw ET, Li Z, Kawi S. Kinetic and mechanistic aspects for CO_2 reforming of methane over Ni based catalysts. Chem Eng J 2015;278:62–78.

[24] Lee SS, Zhu H, Contreras EQ, Prakash A, Puppala HL, Colvin VL. High temperature decomposition of cerium precursors to form ceria nanocrystal libraries for biological applications. Chem Mater 2012;24:424–32. http://dx.doi.org/10.1021/cm200863q.

[25] Jacobs G, Das TK, Zhang Y, Li J, Racoillet G, Davis BH. Fischer–Tropsch synthesis: support, loading, and promoter effects on the reducibility of cobalt catalysts. Appl Catal A Gen 2002;233:263–81. http://dx.doi.org/10.1016/S0926-860X(02)00195-3.

[26] Ma WP, Ding YJ, Lin LW. Fischer-Tropsch synthesis over activated-carbon-supported cobalt catalysts: effect of Co loading and promoters on catalyst performance. Ind Eng Chem Res 2004;43:2391–8. http://dx.doi.org/10.1021/Ie034116q.

[27] Brunauer S, Emmett PH, Teller E. Adsorption of gases in multimolecular layers. J Am Chem Soc 1938;60:309–19. http://dx.doi.org/10.1021/ja01269a023. doi:citeulike-article-id:4074706\r.

[28] Barrett EP, Joyner LG, Halenda PP. The determination of pore volume and area distributions in porous substances. I. Computations from nitrogen isotherms. J Am Chem Soc 1951;73:373–80. http://dx.doi.org/10.1021/ja01145a126.

[29] Pereñiguez R, Gonzalez-delaCruz VM, Caballero A, Holgado JP. $LaNiO_3$ as a precursor of Ni/La_2O_3 for CO_2 reforming of CH_4: effect of the presence of an amorphous NiO phase. Appl Catal B Environ 2012;123–124:324–32. http://dx.doi.org/10.1016/j.apcatb.2012.04.044.

[30] Rahemi N, Haghighi M, Babaluo AA, Jafari MF, Estifaee P. Plasma assisted synthesis and physicochemical characterizations of Ni-Co/Al_2O_3 nanocatalyst used in dry reforming of methane. Plasma Chem Plasma Process 2013;33:663–80. http://dx.doi.org/10.1007/s11090-013-9460-x.

[31] Sutthiumporn K, Kawi S. Promotional effect of alkaline earth over Ni–La_2O_3 catalyst for CO_2 reforming of CH_4: role of surface oxygen species on H_2 production and carbon suppression. Int J Hydrogen Energy 2011;36:14435–46. http://dx.doi.org/10.1016/j.ijhydene.2011.08.022.

[32] Cheng CK, Foo SY, Adesina AA. Glycerol steam reforming over bimetallic Co-Ni/Al_2O_3. Ind Eng Chem Res 2010;49:10804–17. http://dx.doi.org/10.1021/ie100462t.

[33] Ihli J, Wong WC, Noel EH, Kim Y-Y, Kulak AN, Christenson HK, et al. Dehydration and crystallization of amorphous calcium carbonate in solution and in air. Nat Commun 2014;5:3169. http://dx.doi.org/10.1038/ncomms4169.

[34] Foo SY, Cheng CK, Nguyen T-H, Adesina AA. Kinetic study of methane CO_2 reforming on Co–Ni/Al_2O_3 and Ce–Co–Ni/Al_2O_3 catalysts. Catal Today 2011;164:221–6. http://dx.doi.org/10.1016/j.cattod.2010.10.092.

[35] Gallego S, Batiot-dupeyrat C, Mondrago F. Dual active-site mechanism for dry methane reforming over Ni/La_2O_3 produced from $LaNiO_3$ perovskite. Ind Eng Chem Anal Ed 2008;47:9272–8. http://dx.doi.org/10.1021/ie800281t.

[36] Bradford MCJ, Vannice MA. Catalytic reforming of methane with carbon dioxide over nickel catalysts II. Reaction kinetics. Appl Catal A Gen 1996;142:97–122. http://dx.doi.org/10.1016/0926-860X(96)00066-X.

[37] Wei J, Iglesia E. Isotopic and kinetic assessment of the mechanism of reactions of CH_4 with CO_2 or H_2O to form synthesis gas and carbon on nickel catalysts. J Catal 2004;224:370–83. http://dx.doi.org/10.1016/j.jcat.2004.02.032.

[38] Cui Y, Zhang H, Xu H, Li W. Kinetic study of the catalytic reforming of CH_4 with CO_2 to syngas over Ni/α-Al_2O_3 catalyst: the effect of temperature on the reforming mechanism. Appl Catal A Gen 2007;318:79–88. http://dx.doi.org/10.1016/j.apcata.2006.10.044.

[39] Pichas C, Pomonis P, Petrakis D, Ladavos A. Kinetic study of the catalytic dry reforming of CH_4 with CO_2 over $La_2{-}xSr_xNiO_4$ perovskite-type oxides. Appl Catal A Gen 2010;386:116–23. http://dx.doi.org/10.1016/j.apcata.2010.07.043.

[40] Gallego S, Batiot-dupeyrat C, Mondrago F. Dual active-site mechanism for dry methane reforming over Ni/La_2O_3 produced from $LaNiO_3$ perovskite. Ind Eng Chem Anal Ed 2008;47:9272–8. http://dx.doi.org/10.1021/ie800281t.

[41] Foo SY, Cheng CK, Nguyen T-H, Adesina AA. Kinetic study of methane CO_2 reforming on Co–Ni/Al_2O_3 and Ce–Co–Ni/Al_2O_3 catalysts. Catal Today 2011;164:221–6. http://dx.doi.org/10.1016/j.cattod.2010.10.092.

[42] Tsipouriari VA, Verykios XE. Kinetic study of the catalytic reforming of methane with carbon dioxide to synthesis gas over Ni/La_2O_3 catalyst. Catal Today 2001;64:83–90.

[43] Moradi GR, Rahmanzadeh M, Sharifnia S. Kinetic investigation of CO_2 reforming of CH_4 over La–Ni based perovskite. Chem Eng J 2010;162:787–91. http://dx.doi.org/10.1016/j.cej.2010.06.006.

[44] Richardson JT, Paripatyadar SA. Carbon dioxide reforming of methane with supported rhodium. Appl Catal 1990;61:293–309. http://dx.doi.org/10.1016/S0166-9834(00)82152-1.

[45] Wang S, Lu GQ (Max), Millar GJ. Carbon dioxide reforming of methane to produce synthesis gas over metal-supported catalysts: state of the art. Energy & Fuels 1996;10:896–904. http://dx.doi.org/10.1021/ef950227t.

[46] Osaki T, Horiuchi T, Suzuki K, Mori T. Catalyst performance of MoS2 and WS2 for the CO_2-reforming of CH_4 suppression of carbon deposition. Appl Catal A Gen 1997;155:229–38. http://dx.doi.org/10.1016/S0926-860X(96)00391-2.